

Microstructure reconstruction using fiber tracking technique and pore-scale simulations of heterogeneous gas diffusion layer

Liusheng Xiao ^{a,1}, Zequan Yin ^{b,1}, Miaoqi Bian ^a, Nico Bevilacqua ^c, Roswitha Zeis ^c, Jinliang Yuan ^a, Pang-Chieh Sui ^{b,*}

^a Faculty of Maritime and Transportation, Ningbo University, 315211 Ningbo, China

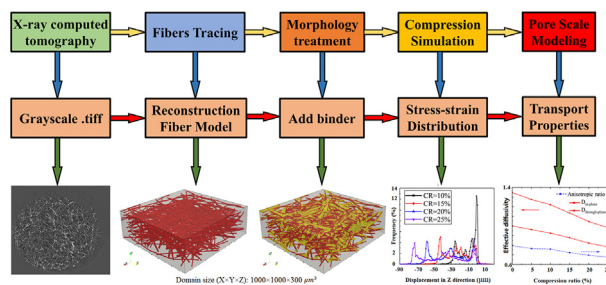
^b School of Automotive Engineering, Wuhan University of Technology, 430070 Wuhan, China

^c Helmholtz Institute Ulm (HIU), Karlsruhe Institute of Technology (KIT), 89081 Ulm, Germany

HIGHLIGHTS

- X-ray computed tomography and fiber tracking are combined for reconstruction.
- Sensitivity analysis of compression speed and Young's modulus is conducted.
- Stress-strain simulations differentiating fiber and binder materials are carried out.
- Anisotropic transport properties of the heterogeneous GDL are investigated.

GRAPHICAL ABSTRACT



ABSTRACT

Two challenging tasks in pore-scale modeling of a gas diffusion layer (GDL) are realistic microstructure reconstruction and stress-strain simulation to differentiate the heterogeneous materials. This study proposes a novel method for reconstructing a GDL using fiber tracking technique and pore-scale modeling to investigate its stress-strain and anisotropic transport properties. X-ray computed tomography, fiber tracking, and morphological processing techniques were employed to reconstruct a realistic GDL. Pore-scale modeling was performed to compute the stress-strain, gas diffusivity, and electrical-thermal conductivity at different compression ratios. The sensitivity of compression speed and Young's modulus were investigated to balance the accuracy and computing cost of stress-strain simulation. The results showed that Young's modulus of 1 GPa and compression speed of 3 m/s meet the requirements for both accuracy and computational cost. The reconstructed GDL showed good agreements with the experimental data when considering fibers' orientation, length, and curvature. It was found that the stress among fibers was approximately five

Keywords:

X-ray computed tomography
Fiber tracking
GDL reconstruction
Stress-strain simulation

* Corresponding author.

E-mail address: pcsui@whut.edu.cn (P.-C. Sui).

¹ The two authors have the same contribution to this study: Liusheng Xiao, and Zequan Yin.

Introduction

Proton exchange membrane fuel cells (PEMFC) are one of the most promising renewable and sustainable energy conversion devices because they have zero pollution during operation [1]. The gas diffusion layer (GDL) is located between the catalyst layer (CL) and bipolar plate (BPP), which performs several roles in gas-water transport, electric-thermal conduction, and mechanical support to protect the membrane. Polyacrylonitrile (PAN) carbon fibers are used as the skeleton of GDLs [2,3]. Phenolic resin [4] was added to bind these carbon fibers closely, and polytetrafluoroethylene (PTFE) was further coated on the surface as a hydrophobic agent [1]. During the operation of a fuel cell, the GDL has three roles: transporting reactants to the CL [5], conducting heat and electrons from the CL [6], and expelling water generated at the cathode CL [7,8]. The effective transport properties of the GDL depend on the local distributions of the carbon fiber, binder, and PTFE, which can be altered by the compressive stress because of the clamping force.

To investigate the effects of compression on the microstructural changes and transport properties of GDLs, some studies have applied X-ray computed tomography (XCT) to observe the microstructural changes of non-uniformly compressed porous media [9,10]. James et al. [11] and Kotaka et al. [12] used XCT to reconstruct the microstructure of GDLs under compression and analyzed its effects on porosity and gas diffusivity. The results show that non-uniform compression has a significant impact on the transport properties of GDLs. However, it is challenging for XCT to differentiate between fibers and binders because of their similar material properties. Moreover, XCT is costly and time consuming. Therefore, simulation techniques were used to study the effect of GDL compression on the transport properties. Su et al. [13] and Zhou et al. [14] found that GDL compression significantly affects the overall performance of the fuel cells. Zhou et al. [15] showed that the contact resistance between GDLs and other components was reduced owing to GDL compression. The transport properties of the GDLs can be significantly affected by compression. The diffusivity and permeability decreased, and the thermal and electrical conductivities increased as the compression ratio of GDLs increased [16–19]. These numerical simulations were carried out at the macroscale, which did not reveal the real fundamental microstructural changes of the GDLs at pore-scale. Therefore, some studies have applied the stochastic reconstruction method to reconstruct the microstructure of GDL [20]. The relationship between microstructural changes and transport properties was further investigated in Refs. [21–24]. Shojaeefard et al. [25] and

Fadzillah et al. [26] indicated that several studies ignored the curvature of carbon fibers during stochastic reconstruction. The fibers were assumed to be straight, which was inaccurate. Thus, it is necessary to find a novel method to utilize the advantages of experimental and numerical methods for GDL reconstruction with high accuracy and low time consumption.

Based on the reconstructed GDL microstructure, a compression simulation is required to obtain compressed GDL models at different compression ratios (CR). Espinoza et al. [27] and Schulz et al. [24] developed a voxel displacement algorithm that assumes that fiber voxels are moved parallel in the through-plane (TP) direction. Gaiselmann et al. [28] applied a vector matrix to represent the new position of the fibers under compression only in the TP direction. Froning et al. [29] assumed that the fibers of the adjacent layers could penetrate each other during compression. However, in practical compression of the GDL, the fibers and binders may contact, bend, extrude and squeeze into the nearby pores dynamically in the TP and in-plane (IP) directions, which should not be simplified or assumed as mentioned earlier. Recently, Xiao et al. [30,31] combined the reconstruction techniques of the finite element method (FEM), and an explicit dynamic method to obtain the three-dimensional (3D) compressed models and stress-strain distributions at different CR. Subsequently, more studies applied FEM and reconstruction techniques to investigate the effects of compression on transport properties [32–34]. Notably, only the fiber and pore phases were considered in the stress-strain simulations, whereas the binder phase was ignored. However, the binder should have non-negligible effects on the stress-strain of the GDLs [35–38].

To utilize the advantages and address the drawbacks of the techniques mentioned above, we propose a new approach that combines XCT, fiber tracking, and morphological processing techniques to reconstruct a more realistic GDL that differentiates fiber and binder materials. FEM and explicit dynamic method are applied to investigate the stress-strain of fibers and binders, and to evaluate the sensitivity of compression speed and Young's modulus at varying compression ratios. A pore-scale model (PSM) code was used to calculate the anisotropic transport properties of the 3D GDL microstructure. In this approach, the orientation distribution, diameter, number, length, and curvature of the fibers are considered for GDL reconstruction. In addition, fiber and binder materials were differentiated for stress-strain simulation. Dynamic contact, bending, and extrusion phenomena during compression were also considered.

The remaining sections of this work are organized as follows: The governing equations for the fiber tracking,

reconstruction method, explicit dynamic FEM and PSM are described in Section [Model Development](#). The sensitivity analysis of the compression speed and Young's modulus, GDL reconstruction, 3D stress-strain distributions for both fibers and binders, effective gas diffusivity, and effective electrical-thermal conductivity are discussed in Section [Results and discussion](#), followed by a summary of major conclusions from this study in Section [Conclusions](#).

Model development

In this study, the fiber tracking technique, XCT, and morphological processing techniques were combined to reconstruct the 3D microstructure of the GDL (39AA, SGL, Germany), which accurately reflects the fiber skeleton and binder distribution. The generated GDLs were then used for compression simulation and pore-scale modeling to investigate the stress-strain distribution, gas diffusivity, thermal conductivity, and electrical resistivity at different CR. The workflow of this approach is illustrated in [Fig. 1](#). The fiber skeleton of the GDL is recognized using a cylindrical inter-correlation analysis and fiber tracking method based on a series of 2D gray-scale images obtained by XCT. The 3D microstructures of the fibers and binder were reconstructed using morphological processing techniques. The reconstructed model was then meshed for solid mechanics simulations to obtain the stress-displacement distributions differentiating the fiber and binder materials. The compressed microstructures were then converted into PSM models to calculate the anisotropic transport properties of the GDL, such as gas transport, electron conduction, and heat transfer inside the microstructure at different CR.

Reconstruction of a heterogeneous GDL

The GDL is mainly composed of carbon fibers, binder, and PTFE. To improve the accuracy of the reconstructed GDL, more detailed information on the structural parameters are required, such as the thickness, local porosity, fiber diameter, length, position, orientation and distribution, as well as binder distribution. It can be challenging for the XCT to differentiate between the fibers and binders because of the similar material properties. To meet these requirements however, the fiber tracking technique, SEM, XCT, and morphological processing techniques are combined to reconstruct a realistic GDL, that can be more accurate than the stochastically reconstructed GDL. The fiber tracking technique is an image processing technique that can be used to track all the centerlines of the column fibers based on XCT data that is reconstructed by scanning a realistic GDL, which reflects the distribution of carbon fibers in a spatial location. The SEM was employed to determine the fiber diameter and binder distribution. Morphological processing techniques were used to reconstruct the microstructure of the GDL based on the experimental data.

The principle of the fiber tracking technique as derived from literature [39–41] is divided into two steps. The first step is to calculate the local normalized correlation for tomographic images using the template of a short solid cylinder. The diameter and length of the cylinders are adjusted, and the voxels within the cylinders are grouped using the algorithm, that is, for each voxel, the highest correlation value and direction of the cylinder are stored. The second step is a linear search, which starts from a voxel p extending along the cylinder direction to a length d . For each candidate voxel p_c in the search area, the correlation value is calculated as:

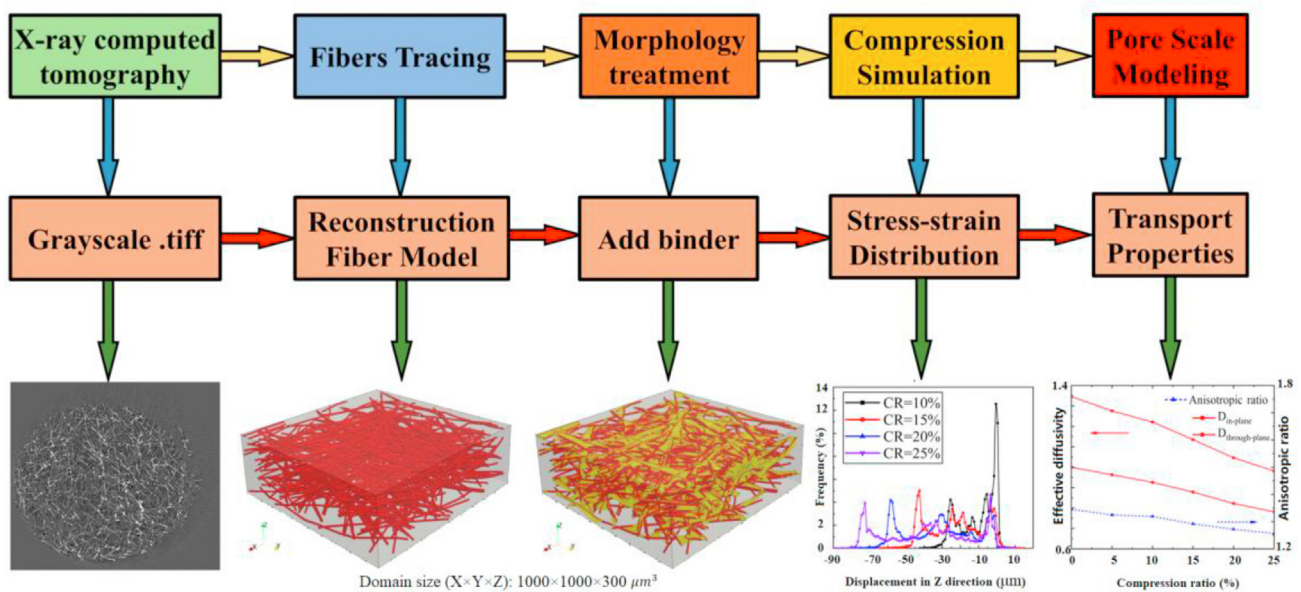


Fig. 1 – Workflow of this study.

$$S(p, p_c) = C(p_c)L(p, p_c) \quad (1)$$

where $C(p_c)$ denotes the correlation of the candidate points and $L(p, p_c)$ is defined as:

$$L(p, p_c) = e^{-\frac{\beta+\gamma}{w_0^2}} \quad (2)$$

where w_0 denotes the weight factor, β and γ are the angles between the vectors $p - p_c$ and the direction for the points p and p_c . L is similar to the smoothing term defined by Fischer and Buhmann [40]. The voxel that produces the highest correlation value is chosen as the next point. Using both steps, fiber statistics (that is, orientation and length) and the spatial location of the fiber centerlines are obtained and subsequently used to reconstruct the skeleton of a GDL with the target porosity.

Based on the production process of the GDL and the low static contact angle between binders and fibers, the binder mainly accumulates at the fiber cross position [22,35]. Binder addition can be implemented by the closure operation of morphological processing [42,43], which includes dilation and erosion steps. The dilation operation causes the boundary of an object to expand outwards and fill the void, which is mathematically described as:

$$A \oplus B = \{x | (\widehat{B})_x \cap A \neq \emptyset\} \quad (3)$$

To keep the object as close to its original shape as possible, an erosion operation is applied to eliminate the boundary points, causing them to shrink inward, which can be defined as:

$$A \ominus B = \{x | (B)_x \subseteq A\} \quad (4)$$

A combination of the two operations above can be defined as:

$$A \cdot B = (A \oplus B) \ominus B \quad (5)$$

Disc and sphere shapes are the most desirable and recommended types that can mimic the wettability of the binder in the GDL microstructure [35]. Zhu et al. studied the effect of the disc- and sphere-shaped binders on the transport properties of GDLs, and they noted that the disc-shaped binder showed better agreement with the experimental data [38]. In this study, a disc-shaped binder was used to achieve the specified porosity and pore size distribution (PSD).

Explicit dynamic FEM

The membrane electrode assembly (MEA) undertakes compressive forces owing to the clamping force during assembling [44]. GDLs are more prone to be compressed owing to their porous microstructure. Some studies assumed the GDL to be homogeneous microstructure with fibers that can penetrate each other, and only parallel movement of the fibers in the compression direction was assumed [45]. Xiao et al. [30,31] were the first to combine the explicit dynamics method and FEM to compute the stress-strain distributions of carbon fibers by considering the dynamic contact, frictional motion and extrusion deformation among fibers during compression. However, only fiber materials were considered in their model. In this

study, the fiber and binder materials of the heterogeneous GDL were differentiated during the compression simulation, which should render a more realistic microstructure.

This study conducted explicit dynamic simulations with the assumptions of continuity, complete elasticity, homogeneity, and isotropy of the materials in the model. The GDL is a porous structure composed of carbon fiber, binder, PTFE and pores. The orientation of the fibers, local concentration and distribution of these solid materials, as well as pore size distribution of the pore phase are moderately different, thereby resulting into an anisotropy in the microstructure and transport properties. In this section however, explicit dynamic simulations are conducted under the assumption of isotropy. The fiber and binder materials were assumed to be isotropic, which represents an inherent property of the material itself. Therefore, the entire GDL is anisotropic, and the fiber/binder materials inside the GDL are isotropic. The governing equations of the stress-strain simulation in this study included kinematic, geometric, and physical equations.

Kinematic equation:

$$\sigma_{ij} + f_i = \rho \ddot{u} \quad (6)$$

where σ is the stress, ρ is the material density, f_i is the body force owing to the clamping force, and \ddot{u} is the acceleration of the finite element.

Geometric equation:

$$\varepsilon_{ij} = \frac{1}{2} (u_{i,j} + u_{j,i}) \quad (7)$$

where ε is the strain and u is the displacement of fibers and binders.

Physical equations:

$$\begin{cases} \sigma_{ij} = \beta \varepsilon_{kk} \delta_{ij} + 2\mu \varepsilon_{ij} \\ \sigma_{kk} = (3\beta + 2\mu) \varepsilon_{kk} \end{cases} \quad (8)$$

where δ_{ij} is the Kronecher symbol, β and μ are the first and second Lamé constants of the material, respectively, which can be calculated using the following equations:

$$\beta = \frac{E\nu}{(1+\nu)(1-2\nu)} \quad (9)$$

$$\mu = \frac{E}{2(1+\nu)} \quad (10)$$

where E and ν are the modulus of elasticity and Poisson's ratio of the material.

The boundary conditions are:

$$\begin{cases} u_i(x, t) = \bar{u}_i(x, t) \\ p_i(x, t) = \bar{p}_i(x, t) \end{cases} \quad (11)$$

where $\bar{u}_i(x, t)$, $\bar{p}_i(x, t)$ are displacement and stress boundary conditions. $p_i = \sigma_{ij}n_j$.

The initial conditions are:

$$\begin{cases} u(x, 0) = u_0(x) \\ u(x, t_1) = u_1(x) \end{cases} \quad (12)$$

where $u_0(x)$ and $u_1(x)$ are the given functions. To solve Equations (6)–(8), the boundary conditions, initial conditions, Hamilton's variation principle, and central difference in time

are combined to obtain the displacement-stress distributions of the fiber and binder materials at every moment.

Pore scale modeling

PSM code was developed [46,47] to evaluate the effective transport properties for species diffusion, electrical conductivity, and heat transfer of deformed GDLs. Gas species, electrons, and heat are transported through pores, carbon fibers and binders, and solid and gas phases, respectively. The Stefan Maxwell formula was used for gas diffusion calculations. Both Fick and Knudsen diffusion were considered [33].

$$\nabla x_{O_2} = \frac{RT}{p} \left(\frac{x_{O_2} j_{H_2O}}{D_{O_2-H_2O}} + \frac{x_{H_2O} j_{O_2}}{D_{O_2-H_2O}} + \frac{x_{O_2} j_{N_2}}{D_{O_2-N_2}} + \frac{x_{N_2} j_{O_2}}{D_{O_2-N_2}} - \frac{j_{O_2}}{D_{O_2,Kn}} \right) \quad (13)$$

$$\nabla x_{H_2O} = \frac{RT}{p} \left(\frac{x_{H_2O} j_{O_2}}{D_{O_2-H_2O}} + \frac{x_{O_2} j_{H_2O}}{D_{O_2-H_2O}} + \frac{x_{H_2O} j_{N_2}}{D_{H_2O-N_2}} + \frac{x_{N_2} j_{H_2O}}{D_{H_2O-N_2}} - \frac{j_{H_2O}}{D_{H_2O,Kn}} \right) \quad (14)$$

$$\nabla x_{N_2} = \frac{RT}{p} \left(\frac{x_{N_2} j_{O_2}}{D_{O_2-N_2}} + \frac{x_{O_2} j_{N_2}}{D_{O_2-N_2}} + \frac{x_{H_2O} j_{N_2}}{D_{H_2O-N_2}} + \frac{x_{N_2} j_{H_2O}}{D_{H_2O-N_2}} - \frac{j_{N_2}}{D_{N_2,Kn}} \right) \quad (15)$$

where x_i is the molar fraction of species i , j_i is the flux of species i , R is the universal gas constant $8.314J/(mol \cdot K)$, T is the temperature, p is the gas pressure, D_{i-j} is the binary diffusivity of species i and j , and D_{i-Kn} is the Knudsen diffusion coefficient of species i . The expressions for the binary and Knudsen diffusion coefficient in this model are listed in Table 1. where p denotes the gas pressure inside the pores of the GDL, d denotes the equivalent diameter of the pores inside the GDL, and T denotes the temperature inside the pores of the GDL. The flux of electrons (current) was calculated using Ohm's law as follows:

$$j_e = \sigma_e \nabla \varphi_e \quad (16)$$

where j_e is the electron flux, σ_e is the electronic conductivity of the material and φ_e is the electron potential. Unlike electrons that can only be conducted through the solid phase, the thermal energy can be transferred in both the solid and gas phases [49]. The heat flux can be determined using Fourier's law as follows:

$$j_T = \lambda \nabla T \quad (17)$$

where j_T is the heat flux and λ is the thermal conductivity of the material. The values of the electrical and thermal conductivities for the fiber and binder material input to the PSM models are summarized in Table 2.

In summary, the equations for the conservation of oxygen, water vapor, electrons and heat are as follows:

Table 1 – Binary diffusion and Knudsen diffusion coefficients [48].

Parameters	Value ($\times 10^{-6} m^2/s$)
$D_{O_2-H_2O}$	$0.282p^{-1} \cdot (T/298.2)^{1.5}$
$D_{O_2-N_2}$	$0.220p^{-1} \cdot (T/293.2)^{1.5}$
$D_{H_2O-N_2}$	$0.293p^{-1} \cdot (T/308.1)^{1.5}$
$D_{O_2,Kn}$	$4850d \cdot (T/32)^{0.5}$
$D_{H_2O,Kn}$	$4850d \cdot (T/18)^{0.5}$
$D_{N_2,Kn}$	$4850d \cdot (T/28)^{0.5}$

Table 2 – Electrical and thermal conductivity of materials [50,51].

Materials	$\sigma_e / (\times 10^3 S/m)$	$\lambda / (W/(m \cdot K))$
Fiber	60	80
Binder	22	37

$$\nabla j_{O_2} = 0 \quad (18)$$

$$\nabla j_{H_2O} = 0 \quad (19)$$

$$\nabla j_e = 0 \quad (20)$$

$$\nabla j_T = S_{ohm} \quad (21)$$

where S_{ohm} is the generated ohmic heat owing to the electron conduction. To solve Equations (18)–(21), the inlet and outlet surfaces were set as Dirichlet boundary conditions and the other four surfaces were set as periodic conditions. The gradient values for gas, electron potential and temperature were set as $0.1 mol/m^3$, $0.001V$ and $0.1K$ respectively [52]. The effective transport properties of the GDL were calculated from the fluxes obtained by the PSM as follows:

$$M_{eff} = \frac{j \cdot l}{b_2 - b_1} \quad (22)$$

where M_{eff} is the effective transport property, j is the flux calculated by the PSM, l is the length of the computational domain, and b_1 and b_2 represent the pre-described boundary conditions.

Results and discussion

Sensitivity analysis of compression speed and Young's modulus

The material and mechanical parameters have different effects on the FEM compression simulations. Previously, the authors have performed a sensitivity analysis of the density, Poisson's ratio, and frictional coefficient between the carbon fibers of GDL [30]. This section however investigates the sensitivity of the compression speed and Young's modulus of the fibers. The density and Young's modulus of the fiber and binder in a GDL differ significantly in practical applications. Some studies have reported that the Young's modulus of the macroscopic GDL is within 10 MPa, and the density is within $1000 kg/m^3$ [14,15,19,34], which should not be used in the microscopic scale model. Most of the GDL is prepared using polyacrylonitrile (PAN) based carbon fibers and phenolic resins [2–4], which form a staggered arrangement of fibers after carbonization and graphitization. The fibers are bonded using the binder. Li reported a Young's modulus of 230 GPa and a density of $1.76g/cm^3$ for the Toray PAN-based carbon fibers; but the Young's modulus was found to be increased by increasing the graphitization temperature [53]. A Young's modulus of 210 GPa for carbon fibers was also reported in another study [54]. Ma et al. [55] reported a Young's modulus of 263.5 MPa for phenolic resins after carbonization at $1100^\circ C$,

and Jia et al. [56] applied a density of 1.25g/cm^3 for phenolic resins. To the best of the authors' knowledge, no study has conducted a sensitivity analysis of the compression speed during the compression simulation. Notably, a higher Young's modulus and lower compression speed leads to a much higher consumption of computational resources. To balance the accuracy and computing cost, the effects of Young's modulus and compression speed on the 3D displacement of the microstructure were investigated. The parameters used for the sensitivity analysis are listed in Table 3. The uncompressed thickness of the GDL models for these cases in Table 3 is $100\ \mu\text{m}$. The displacement constraints of 10, 20 and $30\ \mu\text{m}$ (CR = 10, 20, 30%) were applied to the top surface of the GDL models, and the direction of the displacement constraints is downward. The fixed constraints were applied to the bottom surface of the GDL models. CR is defined as the ratio of the thickness change in the TP direction to the uncompressed thickness of a GDL.

The frequency (vertical axis) in Fig. 2 for a given displacement value (horizontal axis) is computed by counting the number of fiber-binder elements falling within a displacement interval ($2\ \mu\text{m}$) and divided by the total mesh number of 8.3 million. Fig. 2(a–c) show the displacement distribution (frequency at different displacement value) at different compression speeds. There are two main peaks in all the curves of the displacement distribution at different compression speeds and CR. The first peak is $0\ \mu\text{m}$, and the second peaks are 10, 20, and $30\ \mu\text{m}$ for CR = 10, 20, and 30%, respectively. More GDL microstructure maintains a displacement of $0\ \mu\text{m}$ as the compression speed increases. As the CR increases or the compression speed decreases, the displacement increases. The curves of displacement distribution with compression speed of 3 and $0.3\ \text{m/s}$ nearly overlap as $\text{CR} > 10\%$, which means that the sensitivity of the compression speed decreases as the CR increases. Therefore, a compression speed of $3\ \text{m/s}$ is sufficiently accurate for stress-strain simulation.

The effects of Young's modulus of the fiber materials on the displacement distribution are shown in Fig. 2(d–f). The Young's modulus of the fiber materials in this study indicates the inherent properties of the material, which will not be changed by compression or compression speed. The Young's modulus of the fiber material is different from that of the entire porous GDL. The changing variable in Fig. 2 (d), (e) or (f) is Young's Modulus of fiber material. The changing variable between Fig. 2 (d), (e) and (f) is different CR. Only the displacement distribution can be changed by the Young's modulus or different CR. Therefore, there is a basis to compare

the effect of the Young's modulus of the fibers on the displacement distribution at different CR. There are two main peaks in all the curves at different Young's modulus and CR. As the Young's modulus of the fibers increases with the same CR, the displacement increases. As the CR increases with the same Young's modulus, the displacement increases. The curves of the displacement distribution for Young's modulus of 1 and $10\ \text{GPa}$ show high coincidence, and become increasingly overlapping as CR increases. The displacement distribution curves of Young's modulus at 1 and $10\ \text{GPa}$ are highly coincident at different CR, except for a slight deviation when $\text{CR} < 10\%$. Therefore, a Young's modulus of $1\ \text{GPa}$ is sufficiently accurate for stress-strain simulation. To obtain a higher accuracy under low CR, experimental data with a Young's modulus of $6.5\ \text{GPa}$ [57] is used for subsequent stress-strain simulations.

Based on the sensitivity analysis above, the final parameters selected for subsequent investigations are listed in Table 4. The compression speed is $3\ \text{m/s}$.

3D structure reconstruction

In this part, fiber tracking technique, SEM, XCT, and morphological processing techniques are combined to reconstruct the 3D microstructure of the GDL 39AA (SGL company, German), which reflects the fiber skeleton and binder distribution accurately. A fiber skeleton with a domain size of $1000 \times 1000 \times 300\ \mu\text{m}^3$ as illustrated in Fig. 3(a) was generated according to the fiber tracking method introduced in Section Reconstruction of a Heterogeneous GDL. It can be observed that the local fiber orientation, density, curvature, and length are different, which are more realistic and accurate. Morphological processing techniques were then applied to generate a disc-shaped binder with a volume fraction of 50% in the solid phase based on the fiber skeleton structure, as shown in Fig. 3(b). The addition of a binder is achieved by image processing based on three-dimensional gray-scale images of the fiber skeleton. The operation of binder addition was completed using AVIZO software. The detailed methods and principles are described in Section Reconstruction of a Heterogeneous GDL. The final microstructure of the multi-phase GDL is illustrated in Fig. 3(c), which was further compared with the experimental 3D microstructure for validation.

Fig. 4(a) compares the pore size distribution (PSD) of the reconstructed model with the experimental data obtained using XCT, which shows a good agreement between them. The diameter of the pores ranges from 40 to $90\ \mu\text{m}$, and the number of pores fluctuates slightly. The local porosity distribution is also an essential method for GDL characterization. Fig. 4(b) compares the local porosity distributions of the reconstructed model with those of the experimental model in the TP direction. The content and position of the binder are highly related to the fiber orientation and concentration, resulting in an average difference of 3% between the curves of the fiber skeleton model without the binder, and the reconstructed model with the binder. A good agreement is found between the reconstructed model and the experimental model. The validated GDL model was then used for subsequent stress-strain simulations.

Table 3 – Parameters of GDL cases used for sensitivity analysis.

Case Number	Density [g/cm^3]	Compression speed [m/s]	Young's modulus [Pa]
case 1	1.76	3	1×10^7
case 2	1.76	3	1×10^8
case 3	1.76	3	1×10^9
case 4	1.76	3	1×10^{10}
case 5	1.76	30	1×10^8
case 6	1.76	0.3	1×10^8

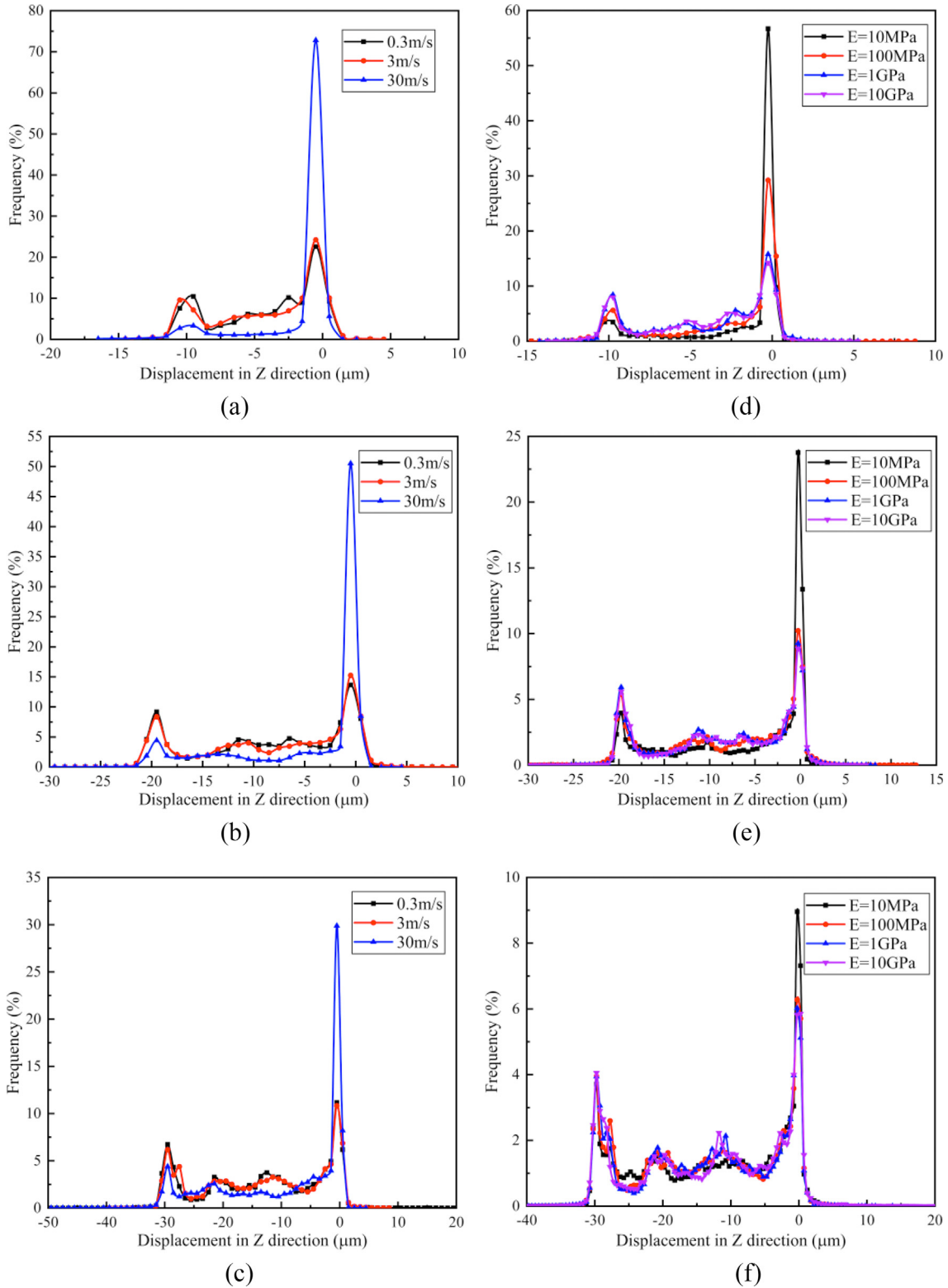


Fig. 2 – The effects of compression speed with (a) CR = 10%, (b) CR = 20%, and (c) CR = 30%, and the effects of Young's modulus with (d) CR = 10%, (e) CR = 20%, and (f) CR = 30% on the displacement distribution.

Stress-strain

In this section, the effect of compression on the stress-strain distribution that differentiates fiber and binder materials at

different CR is investigated, which reflects the dynamic contact, frictional motion, and extruded deformation between fibers and binders during compression. Presumably, this study is the first to consider the dynamic compression process for

Table 4 – Material parameters used for subsequent investigations.

Materials	Frictional coefficient	Young's modulus [Pa]	Poisson's ratio	Density [g/cm ³]
Fiber	0.1	6.5×10^9	0.256	1.76
Binder	0.1	2.65×10^8	0.256	1.25

differentiating fiber and binder materials, which is significant, however challenging.

From the curves of the displacement distribution for fiber-binder materials at different CR in Fig. 5(a), it is evident that there are two main peaks in each curve. The first peak is approximately 0 μm for all curves, and the second peaks are approximately 27, 44, 59 and 73 μm for CR = 10, 15, 20 and 25%, respectively. The displacement increases as the CR increases, and the curves move significantly downward. The displacement ranges for CR = 10, 15, 20 and 25% are (42, +10), (70, +13), (80, +10) and (93, +11) μm , respectively. As the CR increases from 10 to 25%, the displacement increases significantly, and the displacement distribution tends to be more uniform. The displacement and its trend are consistent with those of other studies [30,31]. The fiber and binder materials gradually squeeze into the nearby pores of the middle and bottom areas with increasing CR, which significantly

alters the gas-water transport properties and thermal-electrical conductivity [58,59].

The stress distributions of the fiber and binder at different CR are shown in Fig. 5(b) and (c). As the CR increases, the stress of the fiber and binder increases gradually, and the curves move toward the right-bottom corner. The stress of the fibers ranges from 0 to 50 MPa, and the stress of the binder materials ranges from 0 to 10 MPa. As CR increases from 10 to 25%, the proportion of fiber materials with stress <40 MPa decreases, and binder materials with stress > 5 MPa increases slightly. It is worth noting that the stress of the fibers is approximately five times higher than that of the binders. This is because the Young's modulus of the binder is 265 MPa, and the Young's modulus of the fiber is 6.5 GPa, resulting in higher stress in the fibers and lower stress in the binders at the same strain. This stress-strain simulation can guide heterogeneous GDL design with lower stress and better durability.

Gas diffusivity and electrical-thermal conductivity

The compressed models at different CR from Section Stress-strain are then imported for PSM modeling, including the effective gas diffusivity and thermal-electrical conductivity. Notably, the transport properties computed here are accurate because the compressed microstructures obtained from Section Stress-strain reflect the dynamic contact, frictional

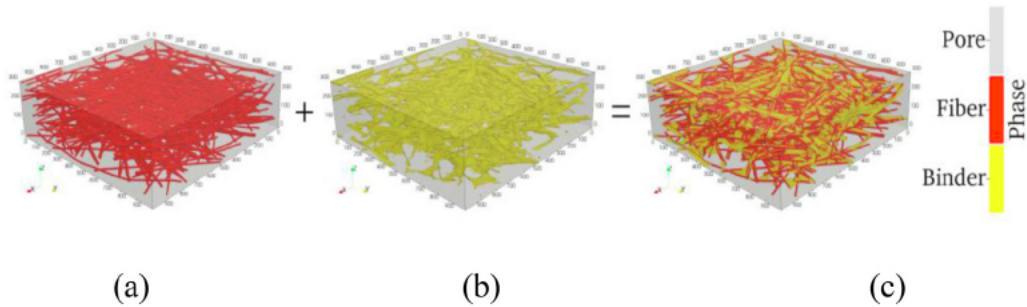


Fig. 3 – 3D rendering of the reconstructed GDL: (a) carbon fiber skeleton, (b) binder structure and (c) heterogeneous GDL.

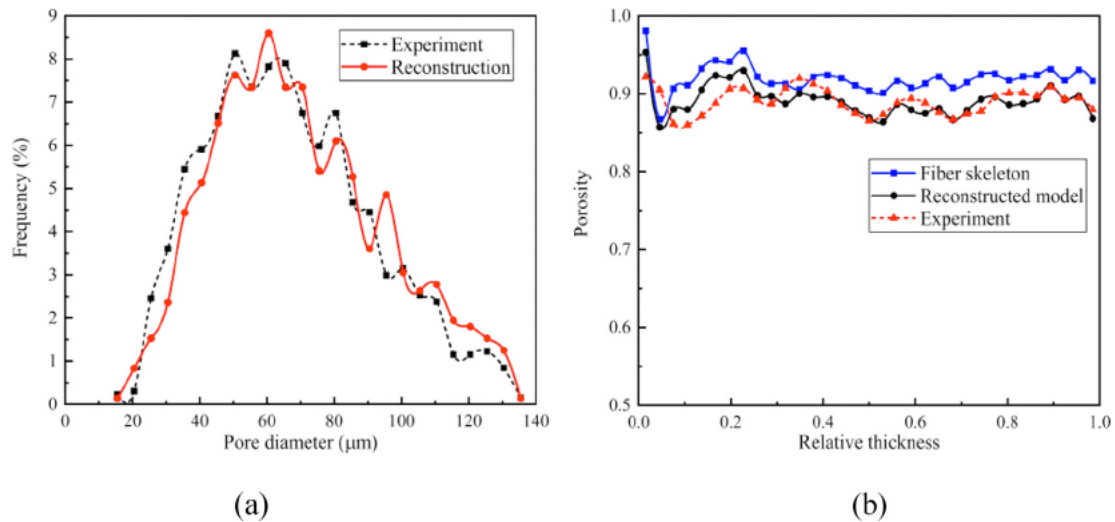
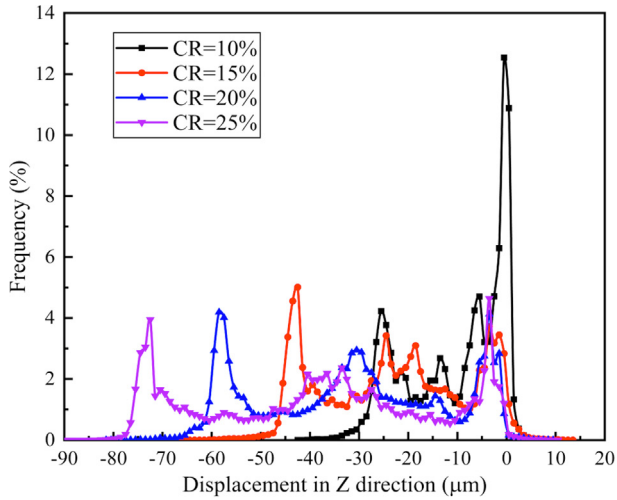
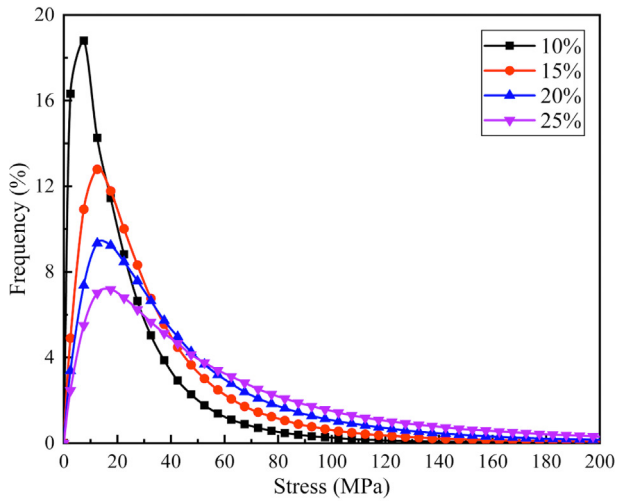


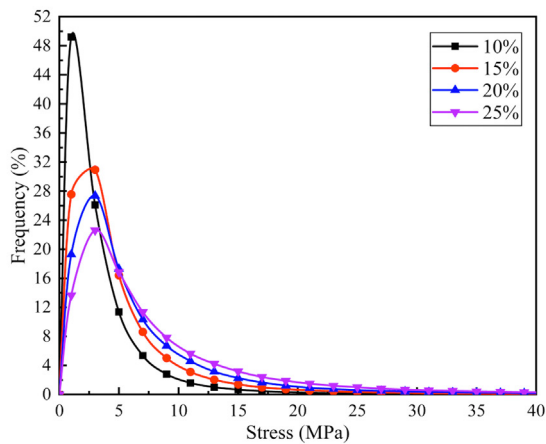
Fig. 4 – (a) Pore size distributions and (b) slice porosity distributions in TP direction.



(a)



(b)



(c)

Fig. 5 – (a) Displacement distribution of the fiber-binder materials in the TP direction, the stress distribution of (b) fiber, and (c) binder at different CR.

motion, and extruded deformation among the fiber and binder materials.

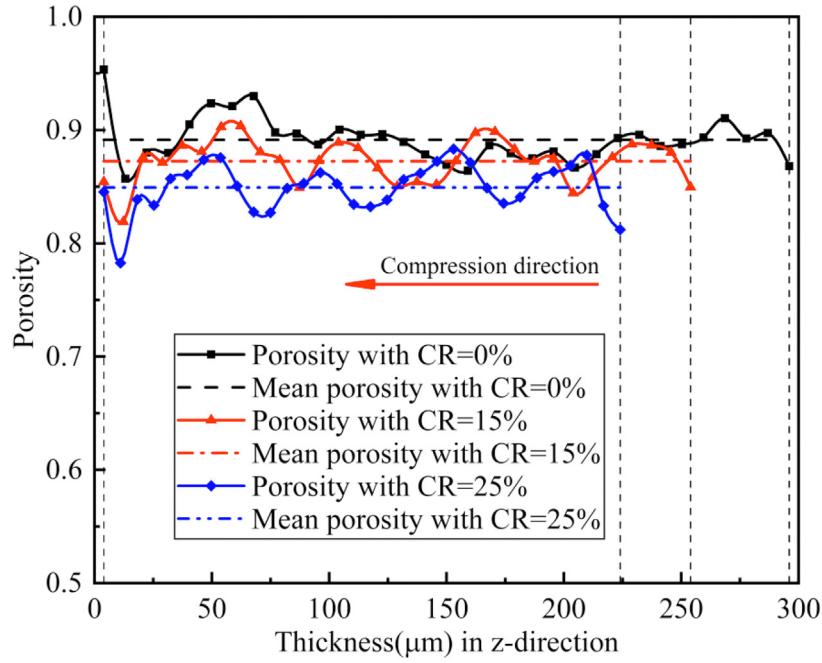
Fig. 6(a) shows a comparison of the local slice porosity along the TP direction (z direction) at different CR. It can be observed that these curves fluctuate significantly along the thickness direction. This is because the fiber materials are distributed layer-by-layer. It is evident from this figure that the local slice porosity generally decreases as the CR increases. This is expected because the fiber-binder materials are compressed and extruded into the lower or upper nearby pores, which results in a decreased fraction of the pore phase. Fiber bending, warpage and extrusion were simulated during the compression simulation in this study, which obtained more accurate GDL models at different CR.

To better compare the results in the TP direction, we adopt the relative effective gas diffusivity and relative effective conductivity in this study. The relative effective diffusivity equals to the ratio of the effective diffusivity to the TP effective diffusivity with a compression ratio of 0%. The relative effective conductivity equals to the ratio of the effective conductivity to the TP effective conductivity with a compression ratio of 0%.

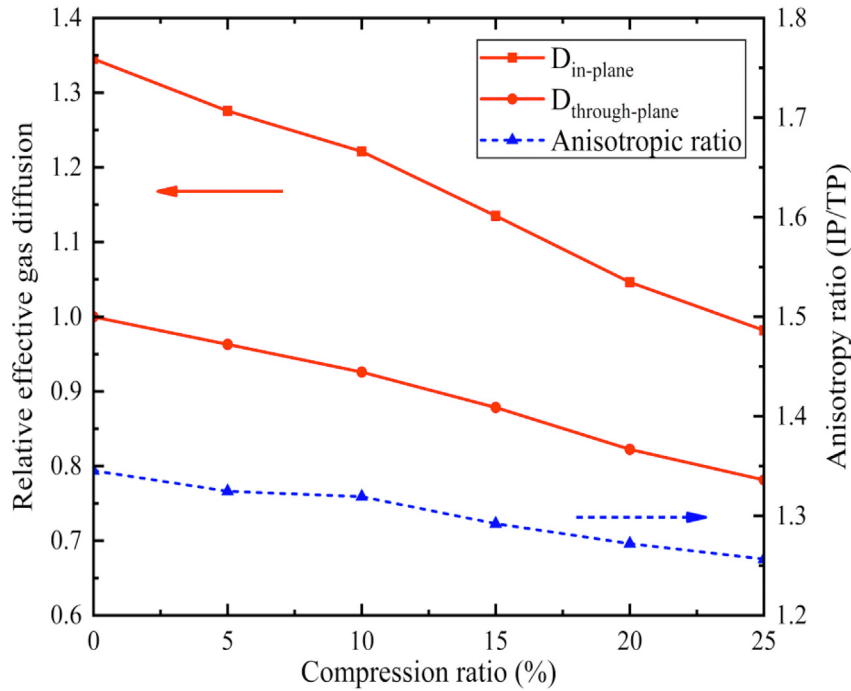
The effective diffusivity in the TP and IP directions decreases as CR increases, as shown in Fig. 6(b). This is expected because of the decreasing porosity and pore size inside the GDL, resulting in more tortuous gas transport pathways. From Fig. 6(b), it can be concluded that the effective diffusivity decreases by approximately 25% as CR increases to 25% in the TP and IP directions. The effective diffusivity in the TP direction is much lower than that in the IP direction, which is the same trend as reported in literature [60]. This is because the fibers are mainly oriented and the binders are fiber-relatively distributed in the IP direction. The anisotropic ratio decreases from 1.35 to 1.25 as CR increases from 0 to 25%, indicating that the GDL microstructure is becoming more isotropic. Here, the anisotropic ratio is defined as the ratio of IP diffusivity to TP diffusivity.

Carbon fibers and binders provide conductive pathways for thermal and electrical applications. As the CR increases, the volume fraction of the solid phase increases, and the continuity and contact area between the solid materials increases, which results in a significant increase in the thermal-electrical conductivity, as shown in Fig. 7(a). As the CR increases from 0 to 25%, the effective electrical-thermal conductivity growth rate in the IP direction is 40%, which is significantly lower than that in the TP direction (300%). The increasing rate of the thermal-electrical conductivity is highly consistent with the data of Devin et al. [61] and Unsworth et al. [62]. The TP conductivity shows a higher sensitivity with increasing CR. This is because more fiber and binder materials are squeezed into the nearby pores during compression, and the contact area of the solid materials in the TP direction increases significantly, resulting in an increase in the solid continuity for conduction in the TP direction.

A comparison between Figs. 6(b) and 7(b) shows that the anisotropic ratios of electrical and thermal conductivity are much higher than those of gas diffusivity. Here, the



(a)

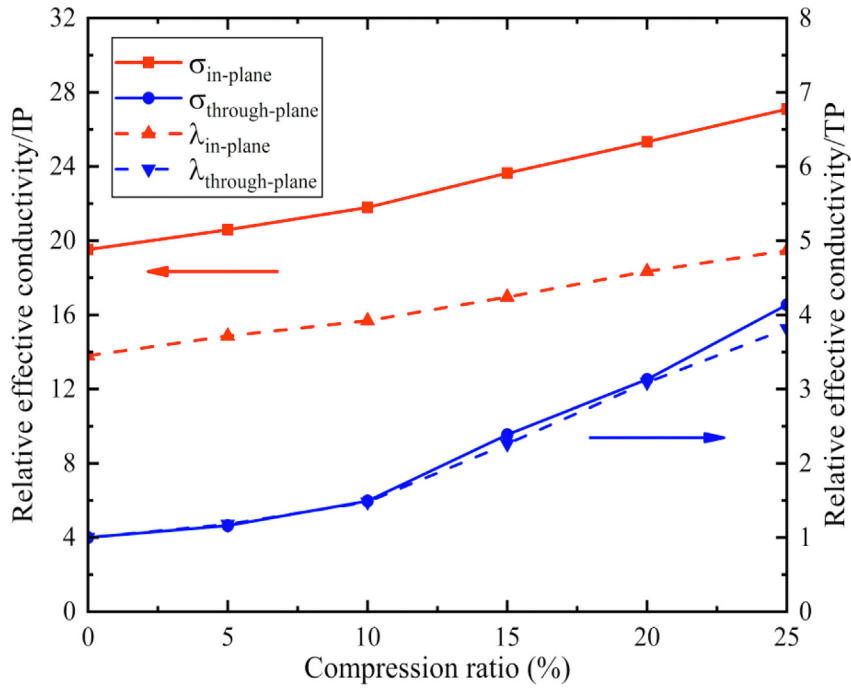


(b)

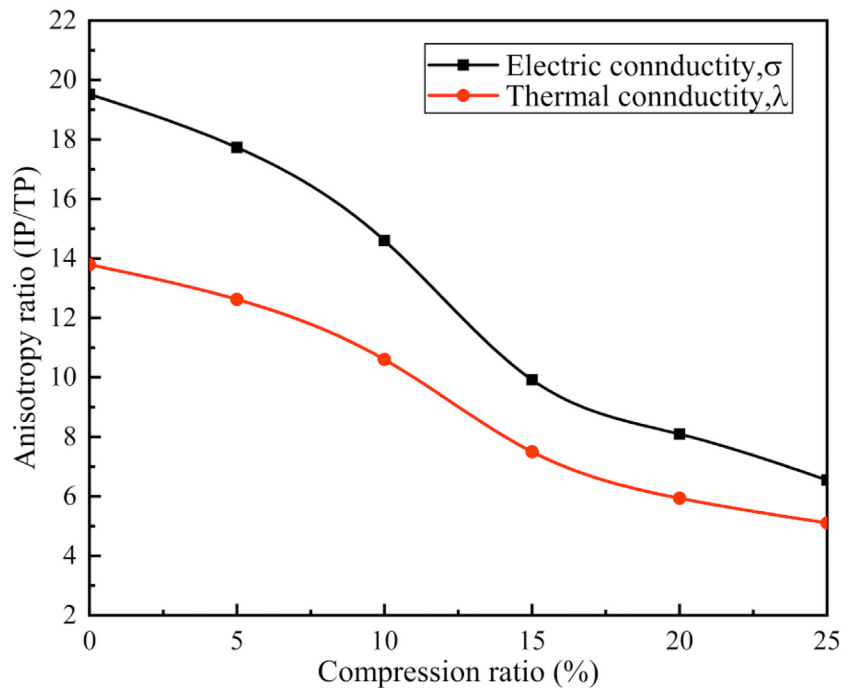
Fig. 6 – (a) Slice porosity along the thickness direction, and (b) effective diffusivity and anisotropic ratio for GDL at different CRs.

anisotropic ratio is defined as the ratio of IP conductivity to TP conductivity. As CR increases, the anisotropic ratio of electrical and thermal conductivity decreases from 19.5 to 6.5, and 13.8 to 5.1, respectively. This indicates that the IP conductivity is much higher than the TP conductivity. This is because the fibers are mainly oriented, the binders are fiber-relatively

distributed in the IP direction, and the continuity of solid materials in the IP direction is significantly better. The anisotropic ratio of thermal conductivity is lower than that of electrical conductivity. This is because heat can transfer through both pores and solid materials, whereas electrons can only conduct through solid materials.



(a)



(b)

Fig. 7 – (a) Effective electrical-thermal conductivity and (b) anisotropic ratios of GDL at different CR.

Conclusions

In this study, the sensitivity of compression speed and Young's modulus of fibers were investigated to balance the accuracy and computing cost for stress-strain simulations.

Then, the fiber tracking technique, SEM, XCT, and morphological processing techniques were combined to reconstruct the actual microstructure of the GDL, which reflects the fiber skeleton and binder distribution. FEM and explicit dynamics methods were combined to simulate the stress-strain

distributions that differentiate between the fibers and binders inside the GDL. During compression, the dynamic contact, frictional motion, and extruded deformation among the fibers and binders were considered. Based on these compressed GDL models at different CR, PSM modeling was performed to investigate the effects of mechanical compression on transport properties. This study can guide a heterogeneous GDL design with lower stress and higher performance. The main findings are as follows:

- (1) A Young's modulus of 1 GPa and compression speed of 3 m/s meet the requirements of both accuracy and computing cost for stress-strain simulations.
- (2) Fiber tracking combined with XCT and morphological processing techniques can provide an accurate reconstruction of GDLs, which reflects the fiber orientation, length, number, position, and curvature.
- (3) The stress of the fibers is approximately five times higher than that of the binders because of the higher Young's modulus of the fibers. The fiber-binder materials gradually squeeze into the nearby pores in the adjacent layers inside the GDL under compression.
- (4) As CR increases to 25%, the effective diffusivity decreases, and the anisotropic ratios decrease from 1.35 to 1.25. The effective electrical-thermal conductivity increases significantly, and the anisotropic ratios of electrical and thermal conductivity decrease from 19.5 to 6.5, and 13.8 to 5.1, respectively.

Declaration of competing interest

The authors declare that they have no known competing financial interests or personal relationships that could have appeared to influence the work reported in this paper.

Acknowledgments

The authors gratefully acknowledge financial support from the National Natural Science Foundation of China (No. 52106254 and 21776226), and Chinesisch-Deutsche Zentrum für Wissenschaftsförderung (M-0070).

REFERENCES

- [1] Majlan EH, Rohendi D, Daud WRW, Husaini T, Haque MA. Electrode for proton exchange membrane fuel cells: a review. *Renew Sustain Energy Rev* 2018;89:117–34.
- [2] Liao YK, Ko TH, Liu CH. Performance of a polymer electrolyte membrane fuel cell with fabricated carbon fiber cloth electrode. *Energy Fuel* 2008;22:3351–4.
- [3] Kim S, Kuk YS, Chung YS, Jin FL, Park SJ. Preparation and characterization of polyacrylonitrile-based carbon fiber papers. *J Ind Eng Chem* 2014;20:3440–5.
- [4] Hung CH, Chiu CH, Wang SP, Chiang IL, Yang H. Ultra thin gas diffusion layer development for PEMFC. *Int J Hydrogen Energy* 2012;37:12805–12.
- [5] Lee SJ, Lee CY, Yang KT, Lee YM, Chang YJ, Ho CL. The surface morphology effects of a metallic bipolar plate on the interfacial contact resistance of a proton exchange membrane fuel cell. *Int J Green Energy* 2013;10:739–53.
- [6] Owejan JP, Trabold TA, Mench MM. Oxygen transport resistance correlated to liquid water saturation in the gas diffusion layer of PEM fuel cells. *Int J Heat Mass Tran* 2014;71:585–92.
- [7] Gostick JT, Fowler MW, Ioannidis MA, Pritzker MD, Volfkovich YM, Sakars A. Capillary pressure and hydrophilic porosity in gas diffusion layers for polymer electrolyte fuel cells. *J Power Sources* 2006;156:375–87.
- [8] Gostick JT, Ioannidis MA, Fowler MW, Pritzker MD. On the role of the microporous layer in PEMFC operation. *Electrochem Commun* 2009;11:576–9.
- [9] Ince UU, Markötter H, George MG, Liu H, Ge N, Lee J, et al. Effects of compression on water distribution in gas diffusion layer materials of PEMFC in a point injection device by means of synchrotron X-ray imaging. *Int J Hydrogen Energy* 2018;43:391–406.
- [10] Tötze C, Manke I, Gaiselmann G, Bohner J, Müller BR, Kupsch A, et al. A dedicated compression device for high resolution X-ray tomography of compressed gas diffusion layers. *Rev Sci Instrum* 2015;86.
- [11] James JP, Choi HW, Pharoah JG. X-ray computed tomography reconstruction and analysis of polymer electrolyte membrane fuel cell porous transport layers. *Int J Hydrogen Energy* 2012;37:18216–30.
- [12] Kotaka T, Tabuchi Y, Mukherjee PP. Microstructural analysis of mass transport phenomena in gas diffusion media for high current density operation in PEM fuel cells. *J Power Sources* 2015;280:231–9.
- [13] Su ZY, Liu CT, Chang HP, Li CH, Huang KJ, Sui PC. A numerical investigation of the effects of compression force on PEM fuel cell performance, vol. 183; 2008. p. 182–92.
- [14] Zhou Y, Jiao K, Du Q, Yin Y, Li X. Gas diffusion layer deformation and its effect on the transport characteristics and performance of proton exchange membrane fuel cell. *Int J Hydrogen Energy* 2013;38:12891–903.
- [15] Zhou P, Wu CW. Numerical study on the compression effect of gas diffusion layer on PEMFC performance. *J Power Sources* 2007;170:93–100.
- [16] Zhou Y, Lin G, Shih AJ, Hu SJ. Multiphysics modeling of assembly pressure effects on proton exchange membrane fuel cell performance. *J Fuel Cell Sci Technol* 2009;6:410051–7.
- [17] Olesen AC, Berning T, Kær SK. The effect of inhomogeneous compression on water transport in the cathode of a proton exchange membrane fuel cell. *J Fuel Cell Sci Technol* 2012;9:1–7.
- [18] Sarkar J, Bhattacharyya S. Investigation of effects of non-homogenous deformation of gas diffusion layer in a PEM fuel cell. *Arch Therm* 2012;33:23–40.
- [19] Liu D, Peng L, Lai X. Effect of dimensional error of metallic bipolar plate on the GDL pressure distribution in the PEM fuel cell. *Int J Hydrogen Energy* 2009;34:990–7.
- [20] Schladitz K, Peters S, Reinel-Bitzer D, Wiegmann A, Ohser J. Design of acoustic trim based on geometric modeling and flow simulation for non-woven. *Comput Mater Sci* 2006;38:56–66.
- [21] Yiotis AG, Kainourgiakis ME, Charalambopoulou GC, Stubos AK. Microscale characterisation of stochastically reconstructed carbon fiber-based Gas Diffusion Layers; Effects of anisotropy and resin content. *J Power Sources* 2016;320:153–67.
- [22] Tayarani-Yoosefabadi Z, Harvey D, Bellerive J, Kjeang E. Stochastic microstructural modeling of fuel cell gas diffusion layers and numerical determination of transport properties

- in different liquid water saturation levels. *J Power Sources* 2016;303:208–21.
- [23] He P, Chen L, Mu YT, Tao WQ. Lattice Boltzmann method simulation of ice melting process in the gas diffusion layer of fuel cell. *Int J Heat Mass Tran* 2020;149.
- [24] Schulz VP, Becker J, Wiegmann A, Mukherjee PP, Wang C-Y. Modeling of two-phase behavior in the gas diffusion medium of PEFCs via full morphology approach. *J Electrochem Soc* 2007;154:B419.
- [25] Shojaeefard MH, Molaieimaneh GR, Nazemian M, Moqaddari MR. A review on microstructure reconstruction of PEM fuel cells porous electrodes for pore scale simulation. *Int J Hydrogen Energy* 2016;98:1–18.
- [26] Fadzillah DM, Rosli MI, Talib MZM, Kamarudin SK, Daud WRW. Review on microstructure modelling of a gas diffusion layer for proton exchange membrane fuel cells. *Renew Sustain Energy Rev* 2017;77:1001–9.
- [27] Espinoza Mayken, Andersson Martin, Yuan J, Sundén B. Compress effects on porosity, gas-phase tortuosity, and gas permeability in a simulated PEM gas diffusion layer. *Arch Therm* 2012;33:23–40.
- [28] Gaiselmann G, Tötze C, Manke I, Lehnert W, Schmidt V. 3D microstructure modeling of compressed fiber-based materials. *J Power Sources* 2014;257:52–64.
- [29] Froning D, Brinkmann J, Reimer U, Schmidt V, Lehnert W, Stolten D. 3D analysis, modeling and simulation of transport processes in compressed fibrous microstructures, using the Lattice Boltzmann method. *Electrochim Acta* 2013;110:325–34.
- [30] Xiao L, Luo M, Zhang H, Zeis R, Sui P-C. Solid mechanics simulation of reconstructed gas diffusion layers for PEMFCs. *J Electrochem Soc* 2019;166:F377–85.
- [31] Xiao L, Luo M, Zhu L, Duan K, Bevilacqua N, Eifert L, et al. Pore-scale characterization and simulation of porous electrode material for vanadium redox flow battery: effects of compression on transport properties. *J Electrochem Soc* 2020;167:110545.
- [32] Zhou X, Niu Z, Bao Z, Wang J, Liu Z, Yin Y, et al. Two-phase flow in compressed gas diffusion layer: finite element and volume of fluid modeling. *J Power Sources* 2019;437:226933.
- [33] Zhu L, Zhang H, Xiao L, Bazylak A, Gao X, Sui P. Pore-scale modeling of gas diffusion layers : effects of compression on transport properties. *J Power Sources* 2021;496:229822.
- [34] Bao Z, Li Y, Zhou X, Gao F, Du Q, Jiao K. Transport properties of gas diffusion layer of proton exchange membrane fuel cells: effects of compression. *Int J Heat Mass Tran* 2021;178:121608.
- [35] Simaafrookhteh S, Shakeri M, Baniassadi M, Sahraei AA. Microstructure reconstruction and characterization of the porous GDLs for PEMFC based on fibers orientation distribution. *Fuel Cell* 2018;18:160–72.
- [36] Simaafrookhteh S, Taherian R, Shakeri M. Stochastic microstructure reconstruction of a binder/carbon fiber/ expanded graphite carbon fiber paper for PEMFCs applications: mass transport and conductivity properties. *J Electrochem Soc* 2019;166:F3287–99.
- [37] Didari S, Asadi A, Wang Y, Harris TAL. Modeling of composite fibrous porous diffusion media. *Int J Hydrogen Energy* 2014;39:9375–86.
- [38] Zhu L, Yang W, Xiao L, Zhang H, Gao X, Sui P-C. Stochastically modeled gas diffusion layers: effects of binder and polytetrafluoroethylene on effective gas diffusivity. *J Electrochem Soc* 2021;168:14514.
- [39] Roseman AM. Particle finding in electron micrographs using a fast local correlation algorithm. *Ultramicroscopy* 2003;94:225–36.
- [40] Weber B, Greenan G, Prohaska S, Baum D, Hege HC, Müller-Reichert T, et al. Automated tracing of microtubules in electron tomograms of plastic embedded samples of *Caenorhabditis elegans* embryos. *J Struct Biol* 2012;178:129–38.
- [41] Rigort A, Günther D, Hegerl R, Baum D, Weber B, Prohaska S, et al. Automated segmentation of electron tomograms for a quantitative description of actin filament networks. *J Struct Biol* 2012;177:135–44.
- [42] Haralick RM, Sternberg SR. Image analysis morphology. *Analysis* 1987:532–50.
- [43] Wang J, Pan Y, Li Y, Zhao L. Quantitative analysis on mathematical morphology. In: *Proc Int Conf Anti-Counterfeiting, Secur Identification. ASID*; 2018. p. 103–6. 2018-Novem.
- [44] Zhou Y, Lin G, Shih AJ, Hu SJ. Assembly pressure and membrane swelling in PEM fuel cells. *J Power Sources* 2009;192:544–51.
- [45] Zamel N, Li X, Shen J, Becker J, Wiegmann A. Estimating effective thermal conductivity in carbon paper diffusion media. *Chem Eng Sci* 2010;65:3994–4006.
- [46] Lange KJ, Sui PC, Djilali N. Pore scale modeling of a proton exchange membrane fuel cell catalyst layer: effects of water vapor and temperature. *J Power Sources* 2011;196:3195–203.
- [47] Lange KJ, Sui P-C, Djilali N. Pore scale simulation of transport and electrochemical reactions in reconstructed PEMFC catalyst layers. *J Electrochem Soc* 2010;157:B1434.
- [48] Lange KJ, Sui PC, Djilali N. Using an ILU/deflation preconditioner for simulation of a pemfuel cell cathode catalyst layer. *Commun Comput Phys* 2013;14:537–73.
- [49] Lange KJ, Sui PC, Djilali N. Determination of effective transport properties in a PEMFC catalyst layer using different reconstruction algorithms. *J Power Sources* 2012;208:354–65.
- [50] El Hannach M, Kjeang E. Stochastic microstructural modeling of PEFC gas diffusion media. *J Electrochem Soc* 2014;161:F951–60.
- [51] García-Salaberri PA, Zenyuk IV, Shum AD, Hwang G, Vera M, Weber AZ, et al. Analysis of representative elementary volume and through-plane regional characteristics of carbon-fiber papers: diffusivity, permeability and electrical/thermal conductivity. *Int J Heat Mass Tran* 2018;127:687–703.
- [52] Zhang H, Zhu L, Harandi HB, Duan K, Zeis R, Sui PC, et al. Microstructure reconstruction of the gas diffusion layer and analyses of the anisotropic transport properties. *Energy Convers Manag* 2021;241:114293.
- [53] Li D, Wang H, Wang X. Effect of microstructure on the modulus of PAN-based carbon fibers during high temperature treatment and hot stretching graphitization. *J Mater Sci* 2007;42:4642–9.
- [54] Parikh N, Allen J, Yassar RS. Effect of deformation on electrical properties of carbon fibers used in gas diffusion layer of proton exchange membrane fuel cells. *J Power Sources* 2009;193:766–8.
- [55] Ma T, Wu X, Li G, Yang W. Microstructures and mechanical properties of pyrocarbons produced from phenolic resin with added Ni(NO₃)₂. *N Carbon Mater* 2017;32:138–43.
- [56] Jia Z, Liu Y, Wen P, Huang M, Ni H, Zhu Y, et al. Property of phenolic resin/TiC/graphite composite bipolar plater. *N Chem Mater* 2012;40:61–3.
- [57] Liu J, Niu P, Xue Y, Liang J. Effect of carbonization airflow on the aggregation structure and mechanical properties of polyacrylonitrile based carbon fibers. *J Beijing Univ Chem Technol* 2014;41:51–7.
- [58] Xu G, Lamanna JM, Clement JT, Mench MM. Direct measurement of through-plane thermal conductivity of partially saturated fuel cell diffusion media. *J Power Sources* 2014;256:212–9.

- [59] Tranter TG, Burns AD, Ingham DB, Pourkashanian M. The effects of compression on single and multiphase flow in a model polymer electrolyte membrane fuel cell gas diffusion layer. *Int J Hydrogen Energy* 2015;40:652–64.
- [60] Flückiger R, Freunberger SA, Kramer D, Wokaun A, Scherer GG, Büchi FN. Anisotropic, effective diffusivity of porous gas diffusion layer materials for PEFC. *Electrochim Acta* 2008;54:551–9.
- [61] Todd D, Bennett S, Mérida W. Anisotropic electrical resistance of proton exchange membrane fuel cell transport layers as a function of cyclic strain. *Int J Hydrogen Energy* 2016;41:6029–35.
- [62] Unsworth G, Zamel N, Li X. Through-plane thermal conductivity of the microporous layer in a polymer electrolyte membrane fuel cell. *Int J Hydrogen Energy* 2012;37:5161–9.